


## Formation of the cavity on a planar interface subjected to a perturbed shock wave

Yifeng He (贺一峰) 

*State Key Laboratory for Turbulence and Complex Systems, College of Engineering,  
Peking University, Beijing 100871, China  
and HEDPS-CAPT, Peking University, Beijing 100871, China*

Naifu Peng (鹏乃夫)


*Ecological Engineering Laboratory (ECOL), Institute of Environmental Engineering (IIE), Faculty of  
Architecture, Civil and Environmental Engineering (ENAC), École Polytechnique Fédérale de Lausanne  
(EPFL), 1015 Lausanne, Switzerland  
and HEDPS-CAPT, Peking University, Beijing 100871, China*

Haifeng Li (李海锋)

*Institute of Applied Physics and Computational Mathematics, Beijing 100094, China*

Baolin Tian (田保林)

*Institute of Applied Physics and Computational Mathematics, Beijing 100094, China  
and HEDPS-CAPT, Peking University, Beijing 100871, China*

Yue Yang (杨越) \*

*State Key Laboratory for Turbulence and Complex Systems, College of Engineering,  
Peking University, Beijing 100871, China  
and HEDPS-CAPT, Peking University, Beijing 100871, China*



(Received 17 September 2022; accepted 6 June 2023; published 27 June 2023)

We report the mechanism and modeling for the formation of cavitylike structures on a planar interface subjected to a perturbed shock wave. The cavity is distinguished from bubbles and spikes formed in the standard Richtmyer-Meshkov instability (RMI). The two-dimensional direct numerical simulation is conducted at a range of shock Mach numbers and Atwood numbers. We elucidate the effects of the interfacial vorticity and the shock-induced vorticity on the cavity formation. The interfacial vorticity, which is important in the standard RMI, only has a minor influence on the cavity width in the linear stage. Alternatively, the cavity width is determined by the Mach-stem height when the shock accelerates the interface. A pair of vorticity patches connecting the Mach stem, as a part of the shock-induced vorticity, penetrate the interface to form the cavity via strong shear layers generated by slipstreams during shock propagation. Inspired by this mechanism, we develop a model of the Mach-stem height to estimate the cavity width in the linear stage at various Mach numbers.

DOI: [10.1103/PhysRevFluids.8.063402](https://doi.org/10.1103/PhysRevFluids.8.063402)

---

\*yyg@pku.edu.cn.

## I. INTRODUCTION

The interaction of shock waves and an inhomogeneous medium contains rich fluid dynamics, such as shock deformation, vorticity generation, and turbulent mixing [1]. The shock-accelerated inhomogeneous flow is of importance for the supersonic combustion [2], supernova explosion [3], and inertial confinement fusion [4]. The Richtmyer-Meshkov instability (RMI), as a typical example, is initiated when a shock wave impacts on a perturbed interface between two fluids of different densities [5–8]. Then the interface evolves into spikes and bubbles [9–11].

Distinguished from the standard RMI, a planar interface between two fluids of different densities evolves into cavity- and steplike structures when it is accelerated by a perturbed shock wave [12]. Ishizaki *et al.* [13] conducted a numerical simulation on this instability. Zou *et al.* [12] observed this instability in planar geometry in experiments. Moreover, Liang *et al.* [14] and Zou *et al.* [15] investigated this instability in a converging geometry. In the experiments, perturbed shocks are usually generated via a planar shock diffracting at a cylinder [12,14]. Zhai *et al.* [16] discussed the effects of the number of cylinders and spacing between cylinders on the interfacial evolution. Zhang *et al.* [17] numerically investigated the Mach-number effect and modeled the role of the impulsive perturbation on the instability. Liao *et al.* [18] found that the amplitude growth rate of the interface decreases with increasing Atwood number, which is essentially different from the result in the standard RMI.

Earlier theoretical study on the instability for a perturbed shock accelerating a planar interface focused on modeling statistical quantities using the perturbation expansion method. Although this method can estimate the interfacial growth rate [13,17], the evolution mechanism for this instability, in particular formation of the cavity, is not yet clear. Furthermore, since the vorticity is deposited when the shock accelerates the interface, the vortex-based model [19] is useful in RMI, e.g., the point vortex and vortex ring are used to model RMI [20–22].

In the present study for a planar interface subjected to a perturbed shock, we quantify the cavity structure and elucidate its formation mechanism in terms of vorticity and shock dynamics. The outline of this paper is as follows. The setup of the direct numerical simulation (DNS) is described in Sec. II. Based on DNS results, we elucidate the cavity formation in Sec. III. Then we develop a cavity-width model via shock dynamics in Sec. IV. Some conclusions are drawn in Sec. V.

## II. SIMULATION OVERVIEW

### A. Governing equations and numerical methods

The variable-density, compressible flow is governed by the two-dimensional (2D) multicomponent Navier-Stokes (NS) equations,

$$\frac{\partial \rho}{\partial t} + \nabla \cdot (\rho \mathbf{u}) = 0, \quad (1)$$

$$\frac{\partial(\rho \mathbf{u})}{\partial t} + \nabla \cdot (\rho \mathbf{u} \mathbf{u}) = -\nabla \cdot (p \boldsymbol{\delta} - \boldsymbol{\tau}), \quad (2)$$

$$\frac{\partial(\rho E)}{\partial t} + \nabla \cdot [(\rho E + p) \mathbf{u}] = \nabla \cdot (\boldsymbol{\tau} \cdot \mathbf{u} - \mathbf{q}_c - \mathbf{q}_d), \quad (3)$$

$$\frac{\partial(\rho Y_i)}{\partial t} + \nabla \cdot (\rho Y_i \mathbf{u}) = -\nabla \cdot \mathbf{J}_i. \quad (4)$$

Here,  $\rho$  denotes the mixture density,  $\mathbf{u} = u_x \mathbf{i} + u_y \mathbf{j}$  the velocity,  $p$  the pressure, and  $\boldsymbol{\delta}$  the identity tensor, where  $\mathbf{i}$  and  $\mathbf{j}$  are unit vectors in the  $x$  and  $y$  directions, respectively. Moreover,  $Y_i$  is the mass fraction of species  $i = 1, 2, \dots, N_s$ , where  $N_s$  is the total number of species with  $\sum_{i=1}^{N_s} Y_i = 1$ . Equation (3) is closed with the equation of state for ideal gas,

$$p = \rho \frac{\mathcal{R}}{M} T = \rho e (\gamma - 1), \quad (5)$$

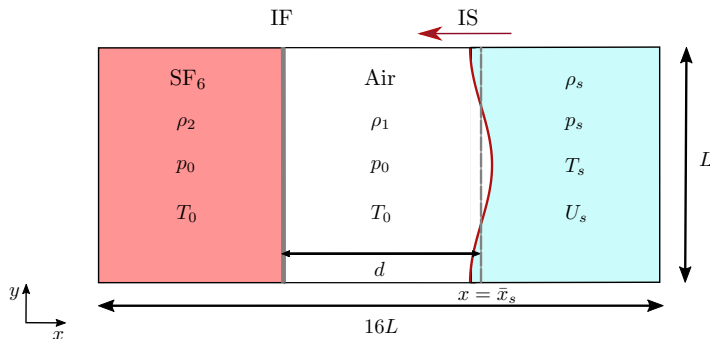


FIG. 1. Schematic diagram of a planar interface (IF) subjected to an initially sinusoidal incident shock (IS) in the computational domain  $\mathcal{D}$ . The IF separates SF<sub>6</sub> and air, and the IS propagates from right to left. The gray dotted line denotes the averaged streamwise position  $\bar{x}_s$  of IS. The distance between IF and  $\bar{x}_s$  is  $d$ .

where  $\mathcal{R}$  is the ideal gas constant,  $M$  the molar mass,  $T$  the temperature,  $\gamma = C_p/C_v$  the specific-heat ratio of the mixture, and  $e$  the internal energy.

In Eq. (3),  $E = e + (\mathbf{u} \cdot \mathbf{u})/2$  denotes the total energy per unit volume, and  $\boldsymbol{\tau} = 2\mu[\mathbf{S} - (\nabla \cdot \mathbf{u})\boldsymbol{\delta}/3]$  denotes the viscous stress tensor, with the mixture viscosity  $\mu$  and the strain-rate tensor  $\mathbf{S}$ . The heat flux  $\mathbf{q}_c = -\nabla(\kappa T)$  is based on Fourier's law with the mixture heat conductivity  $\kappa$ ; the interspecies diffusional heat flux is  $\mathbf{q}_d = \sum_{i=1}^{N_s} C_{p,i} T \mathbf{J}_i$  with Fick's law  $\mathbf{J}_i = -D\rho\nabla Y_i$ , where  $D$  is the mixture diffusion coefficient and  $C_{p,i}$  the constant-pressure specific heat of species  $i$ .

The thermodynamic properties of the mixture are modeled with the isothermal and partial pressure assumptions [23]. For the  $i$ th species, the Sutherland viscosity law is applied to calculate the viscosity as

$$\mu_i = \mu_{r,i} \left( \frac{T}{T_r} \right)^{3/2} \frac{T_r + T_S}{T + T_S}, \quad (6)$$

where  $\mu_{r,i}$  is the reference viscosity at a reference temperature  $T_r$ , and  $T_S$  is an effective temperature.

The present flow has two species. The quantities with subscript 1 or 2 denote those for the air or SF<sub>6</sub>, respectively. In Eq. (6), we set  $T_r = 299.5$  K,  $T_S = 124$  K,  $\mu_{r,1} = 1.7161 \times 10^{-5}$  kg m<sup>-1</sup> s<sup>-1</sup>, and  $\mu_{r,2} = 1.2388 \times 10^{-5}$  kg m<sup>-1</sup> s<sup>-1</sup>. The thermal conductivity  $\kappa_i = C_{p,i}\mu_i/\text{Pr}$  and diffusivities  $D_i = \mu_i/(\rho_i\text{Sc})$  of the  $i$ th species are calculated with the Prandtl number  $\text{Pr} = 0.72$  and Schmidt number  $\text{Sc} = 1.0$ .

Numerical solutions of the NS equations are obtained by using the Adaptive-mesh-refinement Program of Eulerian solvers with X-physics (APEX) [24]. For the convective term, the monotonic upwind scheme for conservation laws with a Riemann solver [25] is used. Other spatial derivatives and gradient terms are evaluated using an eighth-order compact finite-difference scheme. The temporal integration is marched by a third-order Runge-Kutta scheme. The APEX code has been validated and used to investigate the RMI in convergent geometries [24].

## B. DNS setup

As illustrated in Fig. 1, we consider a 2D problem—a perturbed shock wave from the air accelerates a planar interface between still air and SF<sub>6</sub>. The problem is simulated in the domain  $\mathcal{D} = [-8L, 8L] \times [-L/2, L/2]$ . The perturbed shock has a sinusoidal shape as

$$x_s = \bar{x}_s + a_{s0} \cos(2\pi y/L), \quad (7)$$

where  $x_s$ ,  $\bar{x}_s$ ,  $a_{s0}$ , and  $L$  are the streamwise location, averaged streamwise location, amplitude, and wavelength of the shock, respectively. The initial distance between the shock and the interface is  $d$ .

TABLE I. DNS parameters. All cases have  $L = 56$  mm,  $a_{s0} = 5$  mm, and  $\bar{x}_s = 37$  mm.

Ma	1.2			1.8			3.0		
$A$	0.30	0.68	0.80	0.30	0.68	0.80	0.30	0.68	0.80
$\Delta U$ (m/s)	95.10	70.11	57.26	320.03	237.88	195.50	686.82	520.51	433.39
$\Delta t$ (ns)	25	25	25	10	10	10	5	5	5
$N$	1024	1024	1024	4096	4096	4096	2048	2048	2048

For the still air and SF<sub>6</sub>, we set the pressure  $p_0 = 1.013 \times 10^5$  Pa, temperature  $T_0 = 299.5$  K, and density  $\rho_i = p_0 M_i / (\mathcal{R} T_0)$  with the species molar mass  $M_i$ . The postshock quantities (with subscript  $s$ ) are calculated by the Rankine-Hugoniot conditions. The upper and lower boundaries are periodic, and the left and right boundaries are outflow.

To validate the DNS, we set parameter values close to those in the experiment of Liao *et al.* [18], including  $L = 56$  mm,  $d = 45$  mm,  $\bar{x}_s = 37$  mm,  $a_{s0} = 5$  mm, and the shock Mach number  $\text{Ma} = 1.2$  without reshock. The Atwood number  $A = (\rho_2 - \rho_1) / (\rho_1 + \rho_2)$  for the air-SF<sub>6</sub> interface is 0.68 with  $M_1 = 29$  g mol<sup>-1</sup> and  $M_2 = 146$  g mol<sup>-1</sup>.

The initial fields in the shock tube in Fig. 1 are given by

$$\rho(x, y, t = 0) = (\rho_1 - \rho_2)\mathcal{H}[x - (x_s - d)] + (\rho_s - \rho_1)\mathcal{H}(x - x_s) + \rho_2, \quad (8)$$

$$p(x, y, t = 0) = (p_s - p_0)\mathcal{H}(x - x_s) + p_0, \quad (9)$$

$$T(x, y, t = 0) = (T_s - T_0)\mathcal{H}(x - x_s) + T_0, \quad (10)$$

$$\mathbf{u}(x, y, t = 0) = -\mathcal{H}(x - x_s)U_s \mathbf{i}, \quad (11)$$

$$Y_1(x, y, t = 0) = \mathcal{H}[x - (x_s - d)], \quad (12)$$

with a smoothed Heaviside function

$$\mathcal{H}(x) = \frac{1}{2} \left[ \text{erf} \left( \frac{x}{2\delta_0} \right) + 1 \right], \quad (13)$$

the postshock velocity  $U_s$ , and  $\delta_0 = L/128$ . The computational domain is discretized by uniform grid points with the mesh spacing  $\Delta x = L/N$ . The time stepping  $\Delta t$  is chosen to satisfy the Courant-Friedrichs-Lewy condition as listed in Table I. To keep the interface in the middle of  $\mathcal{D}$  during the evolution, the initial velocity in the  $x$  direction is subtracted by  $\Delta U$  to offset the interface translation driven by the shock, where the velocity jump  $\Delta U$  of the interface is evaluated by the one-dimensional Riemann problem [26]. Besides the case with the parameters consistent with the experiment, we conducted a series of DNS at various Ma and  $A$ . The DNS parameters are listed in Table I. Based on the experimental parameters at  $A = 0.68$ , we artificially modify the molar mass of SF<sub>6</sub> to  $M_2 = 54$  g mol<sup>-1</sup> and  $M_2 = 260$  g mol<sup>-1</sup>, corresponding to  $A = 0.30$  and  $A = 0.80$ , respectively.

We conduct a grid convergence test for two typical cases at  $\text{Ma} = 1.2$ ,  $A = 0.68$ , and  $d = 45$  mm with  $N = 256, 512$ , and  $1024$ , and  $\text{Ma} = 3.0$ ,  $A = 0.68$ , and  $d = 25$  mm with  $N = 1024, 2048$ , and  $4096$ , by examining the amplitude of the interface,

$$a_I = |x|_{(Y_1)=0.05} - x|_{(Y_2)=0.05}, \quad (14)$$

where  $\langle \cdot \rangle$  denotes the average over the  $y$  direction. When the shock is accelerating the interface at early times, the growth of  $a_I$  in the second case at a larger Ma is much faster than that in the first case. The plateau of  $a_I$  in the second case is due to the rolling-up of the cavity edge, which will be shown in Sec. III B.

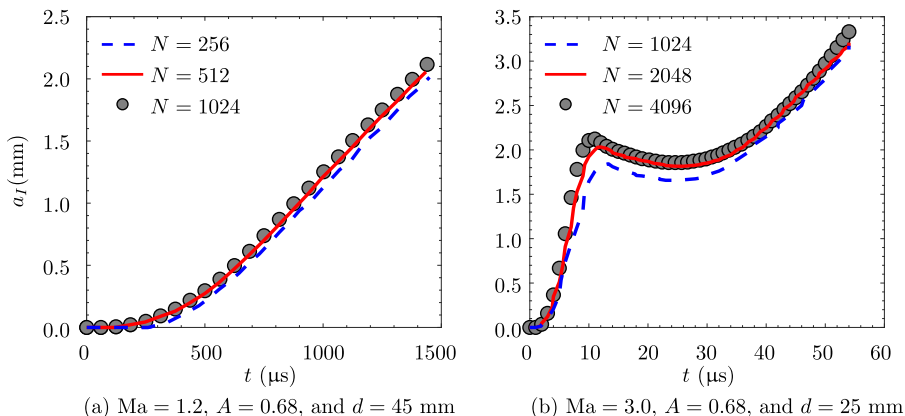


FIG. 2. Temporal evolution of the interface amplitude in the DNS grid convergence test.

Figure 2 shows that the profiles of  $a_I$  converge for  $N = 1024$  at  $Ma = 1.2$  and  $N = 4096$  at  $Ma = 3.0$ , so these resolutions are used in the present study (see Table I). Note that the initial time,  $t = 0$ , is defined when the shock accelerates the interface, which is slightly different from that defined in the experiment [18].

In Fig. 3, the density fields in DNS are in overall good agreement with the experiment results in Fig. 5(c) in Ref. [18]. The step and cavity structures (marked in Fig. 3) occur in both the experiment and DNS. The penetration depth of the cavity in the experiment is slightly smaller than that in DNS due to subtle differences of initial conditions. First, the perturbed shock in the experiment is generated by diffracting a planar shock over a circular cylinder, so its shape is not perfectly sinusoidal. Second, the initial time in the experiment [18] is defined when the shock passes the cylinder center, which is slightly earlier than the initial time in this study.

### III. CAVITY FORMATION

#### A. Shock-induced vorticity

To analyze the vorticity effect on the interface deformation, the temporal evolution of the shock, interface, and generated vorticity is depicted by the numerical schlieren field  $\Phi = \exp$

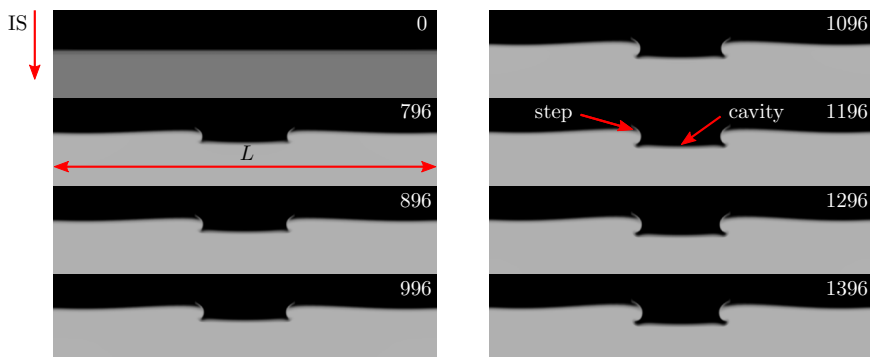


FIG. 3. Evolution of the density field in the DNS (black: air; gray: SF<sub>6</sub>). Measuring times are shown in the upper right corner of each figure in  $\mu\text{s}$ . The corresponding experimental result is shown in Fig. 5(c) in Ref. [18] for comparison. The parameters  $A$  and  $\Delta U$  and measuring times in the present DNS are the same as those in the experiment [18].

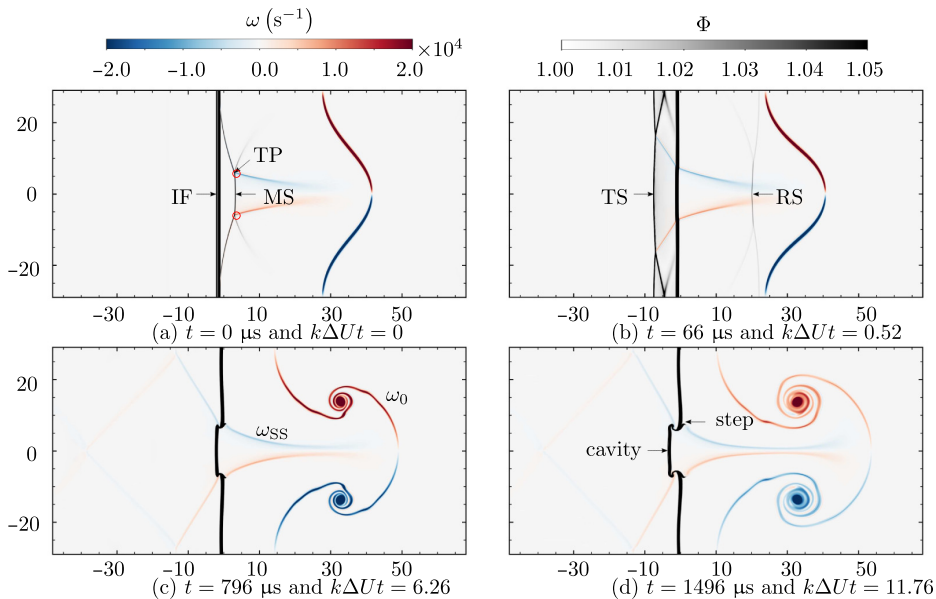


FIG. 4. Evolution of the schlieren (gray) and vorticity (red and blue) fields with  $Ma = 1.2$ ,  $A = 0.68$ , and  $d = 45$  mm. The parameters are consistent with those in the experiment [18]. The units of both axes are in mm. The triple point (TP), Mach stem (MS), transmitted shock (TS), reflected shock (RS), and vorticity patches related to the initial shock ( $\omega_0$ ) and slipstream ( $\omega_{SS}$ ) are marked.

$(1.2|\nabla\rho|/|\nabla\rho|_{\max})$  [27] and the vorticity field  $\omega\mathbf{k} = \nabla \times \mathbf{u}$  in Fig. 4, where  $\mathbf{k}$  denotes the unit vector normal to the  $x$ - $y$  plane, the subscript “max” denotes the global maximum value, and the dimensionless times  $k\Delta Ut$  are listed with  $k = 2\pi/L$ .

In Fig. 4(a), the Mach-reflection structure forms during the propagation of the perturbed shock [28]. It contains a Mach stem and two triple points, as visualized by  $\Phi$  at  $t = 0$  when the shock accelerates the interface. After the shock impacts the interface, transmitted and reflected shocks are generated at  $t = 66 \mu\text{s}$  in Fig. 4(b), and the postshock region is in between [26]. The cavity and step structures form on the interface at  $t = 1496 \mu\text{s}$ , as marked in Fig. 4(d).

In Fig. 4(c), the vorticity contour shows two types of concentrated vorticity patches,  $\omega_0$  and  $\omega_{SS}$ . They have different generating mechanisms. First, the initial shock deposits  $\omega_0$  at the initial position due to the velocity gradient across the shock [see Eq. (11)]. Second, the slipstream downstream to the shock is identified by  $\omega_{SS}$ , as a shear layer spread out from the triple point [29].

Note that the generation of the finite-size vortex sheet  $\omega_0$  is inevitable in the numerical simulation [30], but we find that  $\omega_0$  only has a slight influence on the cavity formation in the linear stage at  $k\Delta Ut \leq 1$ . Its effect is minor by comparing the contributions from  $\omega_0$  and  $\omega_{SS}$  using the Biot-Sarvart law. The normalized variation due to  $\omega_0$  on the cavity width is typically less than 10%.

Figure 5 shows a close-up view of the shock propagation. In Figs. 5(a) and 5(b), the height  $h$  of the Mach stem, i.e., the distance between the two triple points, grows and the amplitude of the shock distortion rapidly decays during the shock propagation. A shock with a nonzero curvature deposits the vorticity  $\omega_{CS}$  downstream [30]. The initial sinusoidal shock leaving behind vorticity  $\omega_0$  in Fig. 5(a) deposits nearly negligible vorticity  $\omega_{CS}$  during the propagation in Fig. 5(b) due to the rapid decay of the shock curvature and amplitude. In Fig. 5(c), after the shock impacts the interface, a small amount of the interfacial vorticity  $\omega_{IF}$  is generated on the interface due to the misalignment of pressure and density gradients [9], as in the standard RMI.

The generating mechanisms of  $\omega_{IF}$ ,  $\omega_{CS}$ , and  $\omega_{SS}$  are illustrated in Fig. 6. The interfacial vorticity  $\omega_{IF}$  is generated by the shock accelerating the interface and it drives the interfacial evolution in the

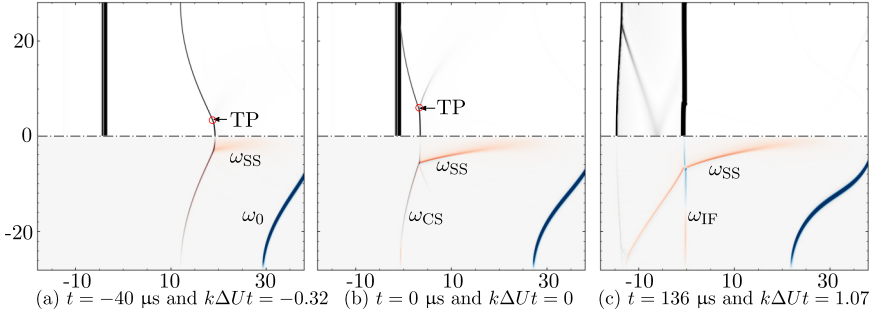


FIG. 5. Close-up view of the schlieren (upper half) and vorticity (lower half) fields during the shock propagation with  $Ma = 1.2$ ,  $A = 0.68$ , and  $d = 45$  mm. The color bars are the same as in Fig. 4.

RMI [21,22]. The shock-induced vorticities  $\omega_{CS}$  and  $\omega_{SS}$  are deposited by the Mach-reflection shock the interface upstream. Both the curved shock and slipstream contribute to the generation of  $\omega_{CS}$  and  $\omega_{SS}$ . Note that the propagating planar shock in the standard RMI [9] before accelerating the interface cannot deposit shock-induced vorticity.

### B. Vorticity effects on cavity formation

We examine the effects of the interfacial vorticity and shock-induced vorticity on the cavity formation. As sketched in Fig. 7, the cavity geometry is characterized by the parameters below, instead of a direct measurement from experimental images [12]. The width  $W$  and the depth  $H$  of the cavity are determined by three points,  $P_A$ ,  $P_B$ , and  $P_C$ . The coordinates of the three points are quantified below:  $P_A$  with  $y_A = 0$  is at the centerline and located at the bottom of the cavity;  $P_B$  with

$$\int_{-L}^L Y_2(x, y_B) dx = \max \left\{ \int_{-L}^L Y_2(x, y) dx \mid 0 \leq y \leq \frac{L}{2} \right\} \quad (15)$$

and

$$Y_2(x_A, y_A) = Y_2(x_B, y_B) = Y_{cr} \quad (16)$$

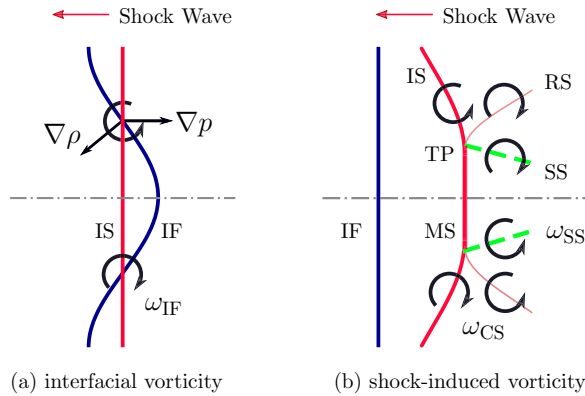


FIG. 6. Schematic diagram for different mechanisms of vorticity generation. Blue line: interface (IF); thick red line: incident shock (IS); thin red line: reflected shock (RS); line segment of IS between two triple points (TPs); Mach stem (MS); green dashed line: slipstream (SS). Note that (b) is essentially a close-up detail of Fig. 4(a).

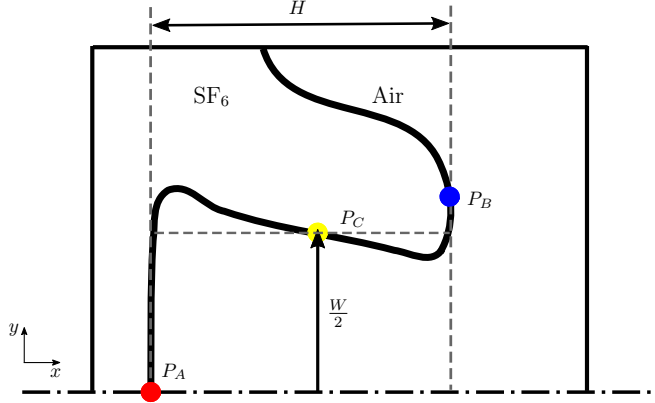


FIG. 7. Schematic diagram of the cavity. The bold black line denotes the interface separating  $\text{SF}_6$  and air. The cavity depth is determined by points  $P_A$  and  $P_B$ , and the cavity width in the linear stage is determined by point  $P_C$  and the symmetric line (dash-dotted line).

is located at the top of the cavity with  $Y_{cr} = 0.95$ ;  $P_C$  with

$$x_C = (1 - \alpha)x_A + \alpha x_B \quad (17)$$

and

$$y_C = \min \left\{ y \mid Y_2(x_C, y) = Y_{cr}, 0 \leq y \leq \frac{L}{2} \right\} \quad (18)$$

is between  $P_A$  and  $P_B$  with a weighting factor  $\alpha = 0.7$ . This value of  $\alpha$  is chosen to measure the largest cavity width. Then,  $W = 2y_C$  and  $H = x_B - x_A$  are obtained, as marked in Fig. 7. In the present study, the cavity width is measured at the time  $t_M = 1/(k\Delta U)$ . This small time is within the period of the incipient cavity formation when  $H$  is small (refer to Fig. 4). We observe that the cavity width is nearly invariant during a short linear stage defined by the period with  $k\Delta U t \leq 1$ .

First, to isolate different vorticity effects, we take the same shock-induced vorticity by setting  $d = 25$  mm, and only vary the interfacial vorticity by artificially modifying the molar mass of  $\text{SF}_6$  to achieve  $A = 0.30$  and  $A = 0.80$  (also see Table I). At the same  $\text{Ma}$  and different  $A$ , the cavity widths are almost the same in Fig. 8. In other words,  $W$  is dependent on the shock-induced vorticity, while almost independent of the interfacial vorticity. At the same  $A$ ,  $W$  varies with  $\text{Ma}$  and is very close to the Mach-stem height. Note that the Mach stem is between the two patches of  $\omega_{SS}$  (see Figs. 4 and 5). The effect of the Mach reflection on the cavity width will be modeled in Sec. IV.

Second, we keep  $A = 0.68$  and only vary  $d$  to investigate effects of the shock-induced vorticity on the cavity formation. All the other parameters are listed in Table I. In Fig 4(a), the Mach-stem height grows with the propagation of the curved shock and the separation of the two Mach-reflection shocks. In addition, the growth of the Mach stem is discussed in detail in Sec. IV. Namely,  $h$  grows as the incident shock propagates from its initial location to the interface (also see Fig. 1), so it increases with  $d$ . Considering  $W$  increases with  $d$  at the same  $\text{Ma}$  in Fig. 9 and  $W \approx h$  in Fig. 8, we demonstrate that the cavity width in the linear stage is determined by the Mach-stem height when the shock accelerates the interface.

Referring to Fig. 6(b), the two slipstreams originating from the triple points have strong shear layers and they penetrate the interface to form the cavity. This mechanism is further illustrated in the close-up view of schlieren and vorticity fields in Fig. 10. Before the shock accelerates the interface, the slipstream, spreading out from the triple point, deposits  $\omega_{SS}$  at the interface upstream in Fig. 10(a). When the slipstream penetrates the interface, the strong shear layer associated with  $\omega_{SS}$  causes the relative motion (marked by red arrows) on two sides of the strip of  $\omega_{SS}$  (marked by red



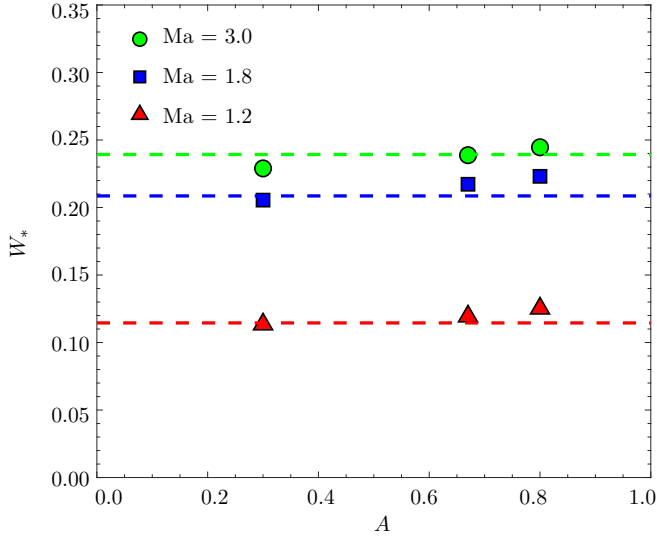


FIG. 8. Dimensionless width  $W_* = W/L$  of the cavity measured at  $t = t_M$  with  $d = 25$  mm and various Ma and  $A$ . The normalized Mach-stem height measured when the shock is impacting on the interface is compared with  $W_*$ .

dashed line) in Fig. 10(b). Under the shearing motion, the cavity forms after the shock accelerates the interface in Fig. 10(c).

With increasing Ma, both shock and cavity structures become more complex. Figure 11 shows the cavity formation at Ma = 1.8 from the shock impact in Fig. 11(a), through the linear stage at  $k\Delta Ut \leq 1$  with small  $H$  in Fig. 11(b), to the nonlinear stage at  $k\Delta Ut > 1$  in Figs. 11(c) and 11(d). The deposited vorticity at Ma = 1.8 is much stronger than that at Ma = 1.2, where the maximum value in the vorticity color bar in Fig. 11 is increased by one order of magnitude from that in Fig. 4.

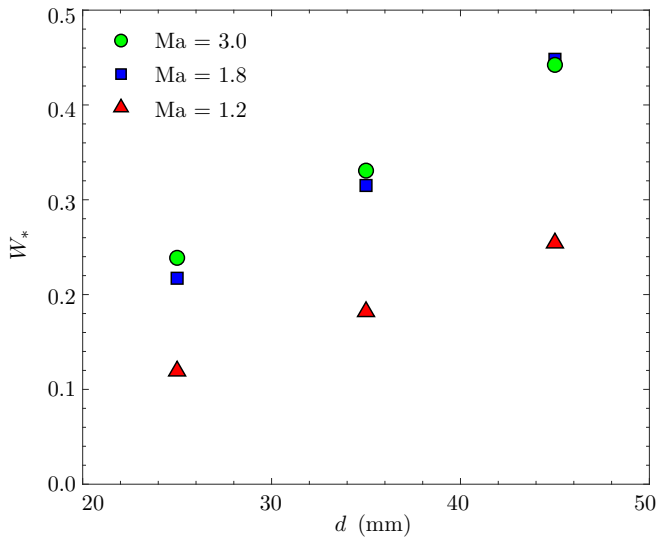


FIG. 9. Dimensionless width  $W_* = W/L$  of the cavity measured at  $t = t_M$  with  $A = 0.68$  and various Ma and  $d$ .

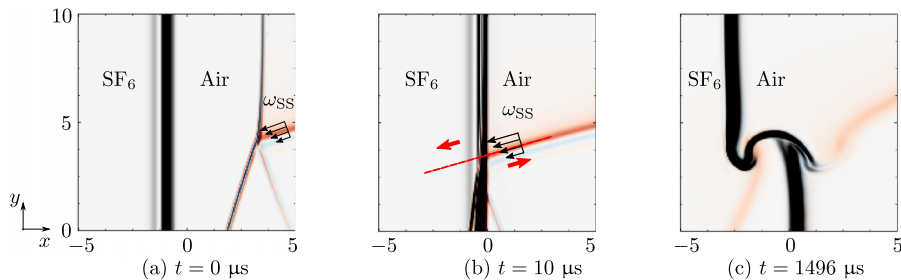


FIG. 10. Close-up view of the schlieren (gray) and vorticity (red and blue) fields in Fig. 4 with  $Ma = 1.2$ ,  $A = 0.68$ , and  $d = 45$  mm. The axes are in units of mm. The red dashed line is along the strip of  $\omega_{SS}$ . The black arrows denote the shear shearing motion associated to  $\omega_{SS}$ . Two red arrows denote the relative motion on two sides of the strip of  $\omega_{SS}$ .

The shock-wave pattern between the interface and transmitted shock in Fig. 11(b) is more complex than that in Fig. 4(b) due to the Guderley reflection with two triple points [31]. Specifically, two slipstreams with  $\omega_{SS}$  (marked by two black arrows) spread downstream of the transmitted shock in Fig. 11(c) instead of one in Fig. 4(c). The strong vortex sheet  $\omega_0$  rolls up into a large-scale mushroomlike structure.

At the nonlinear stage, the cavity width measured at the trailing part of the cavity shrinks due to the entrainment of the mushroomlike  $\omega_0$ , while the width measured at the leading part of the cavity expands due to the Kelvin-Helmholtz instability (KHI) [32] in Figs. 11(d) and 4(d). Since we focus on the cavity formation, most of the present discussion is restricted to the linear stage.

As shown in Fig. 12 for  $Ma = 3.0$ , the interface, shock, and deposited vorticity generate numerous small-scale structures during the cavity formation. Although it appears to be difficult to accurately discern physical and numerical oscillations downstream in Figs. 11 and 12, we find that these small-scale structures have little influence on the cavity geometry using different grid resolutions and numerical schemes.

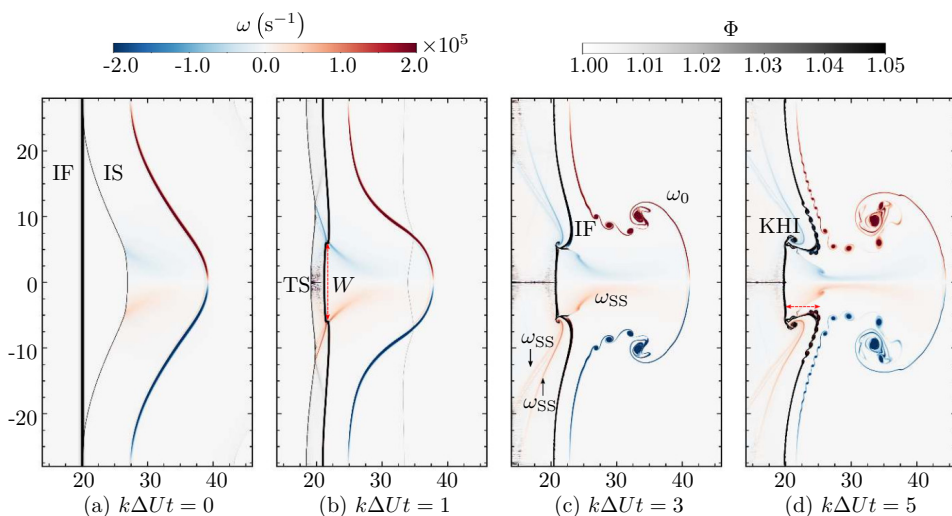


FIG. 11. Evolution of the schlieren (gray) and vorticity (red and blue) fields with  $Ma = 1.8$ ,  $A = 0.68$ , and  $d = 25$  mm. The units of both axes are in mm.

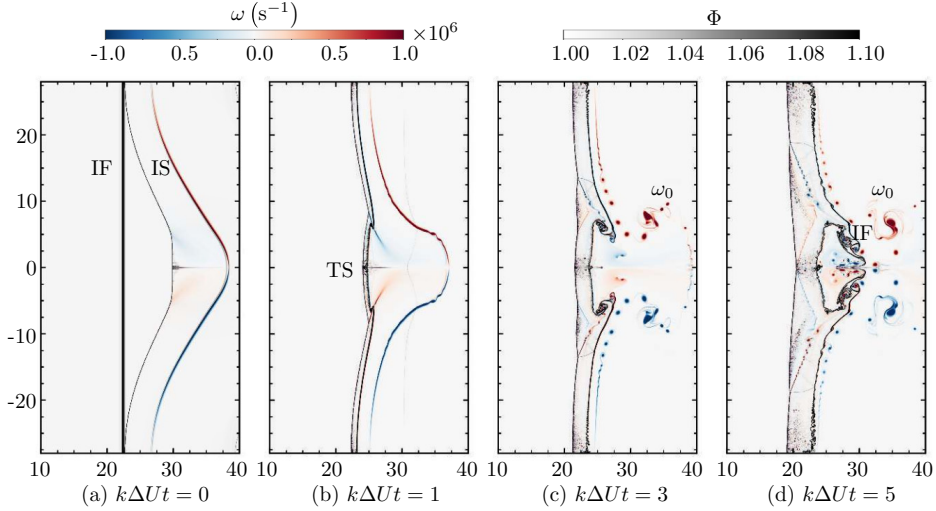


FIG. 12. Evolution of the schlieren (gray) and vorticity (red and blue) fields with  $Ma = 3.0$ ,  $A = 0.68$ , and  $d = 25$  mm. The units of both axes are in mm.

#### IV. MODELING THE CAVITY WIDTH IN THE LINEAR STAGE

Inspired by the formation mechanism of the cavity, we estimate the cavity width in the linear stage via modeling the Mach-stem height  $h$ . This model is based on the assumptions below. First, the process of the shock impacting the interface is fast enough, so that we approximate that the Mach stem moves with the constant speed  $U_{MS}$  and Mach number  $Ma$ . Second, all the segments linked by the triple points in the Mach-reflection shock (see Fig. 6) are assumed to be planar [33]. This assumption is supported by the negligible vorticity deposited by the propagating shock in Fig. 4 [30]. The important modeling ingredients are illustrated in Fig. 13(a). The red lines, from thick to thin, represent the Mach stem, incident shock, and reflected shock, respectively. The three shock segments are linked at the triple point marked by the blue dot.

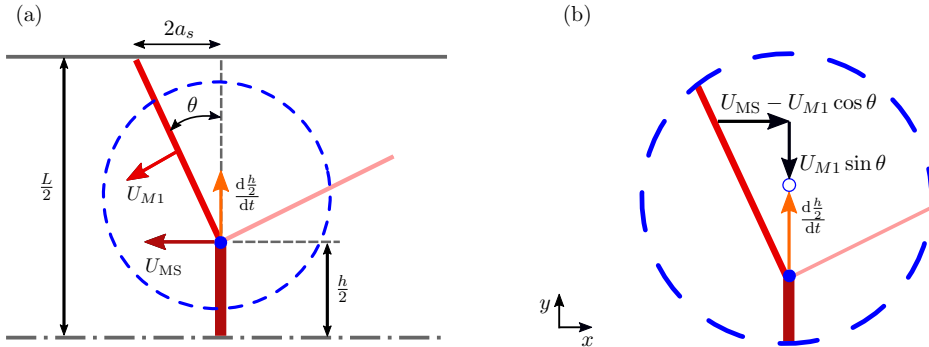


FIG. 13. (a) Schematic diagram for the decompositions of the shock structure and velocity. The red lines, from thick to thin, represent the Mach stem, incident shock, and reflected shock, respectively. The blue solid circle denotes the triple point. (b) Close-up view of the region near the triple point, marked by the blue dashed circle in (a). The triple point moves from the solid circle to the open circle. The velocities marked in (a) and (b) are in the laboratory frame and the relative frame on the moving Mach stem, respectively.

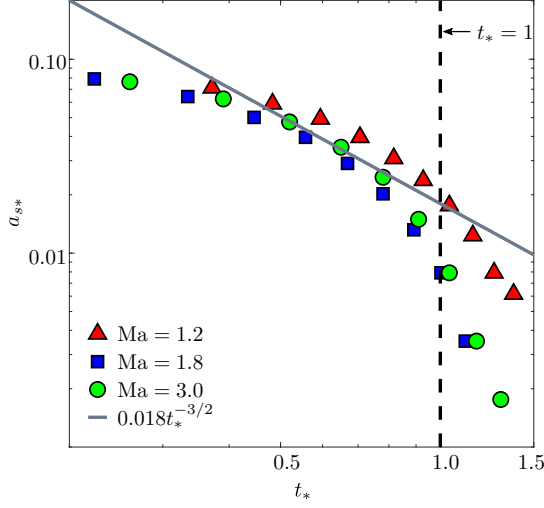


FIG. 14. Decay of the dimensionless shock amplitude in the shock propagation at various Ma, along with the power law fitted by  $a_{s*}$  at  $t_* \leq 1$ .

Next, we model the temporal evolution of  $h$ . In Fig. 13(a), the propagating velocity of the triple point is decomposed into  $U_{MS}$  and  $d(h/2)/dt$  in the laboratory frame. The incident shock with the perturbed amplitude  $a_s$  moves with the speed  $U_{M1}$  and Mach number  $Ma_1$ . The angle  $\theta$  between the incident shock and the Mach stem satisfies

$$\cot \theta = \frac{L - h}{4a_s}. \quad (19)$$

Figure 13(b) depicts a subdomain near the triple point. Taking the reference frame on the moving Mach stem, we decompose the relative velocity of the incident shock into  $x$  and  $y$  components  $U_{MS} - U_{M1} \cos \theta$  and  $U_{M1} \sin \theta$ , respectively. As illustrated in Fig. 13(b), the geometrical relation gives

$$\frac{d\frac{h}{2}}{dt} = \frac{U_{MS} - U_{M1} \cos \theta}{\tan \theta} - U_{M1} \sin \theta. \quad (20)$$

Substituting Eq. (19) and  $U_{M1}/U_{Ma} = Ma_1/Ma$  into Eq. (20) yields

$$\frac{\dot{h}}{U_{MS}} = \frac{L - h}{2a_s} \left( 1 - \frac{Ma_1}{Ma \cos \theta} \right), \quad (21)$$

with  $\dot{h} = dh/dt$ . Using  $L$  and  $U_{MS}$  as the reference length and velocity, respectively, Eq. (21) is nondimensionalized into

$$\dot{h}_* = \frac{1 - h_*}{2a_{s*}} \left( 1 - \frac{Ma_1}{Ma \cos \theta} \right), \quad (22)$$

where the asterisk denotes the dimensionless quantity. As demonstrated in Fig. 14, the evolution of  $a_{s*}$  generally satisfies a power law of  $t_*^{-3/2}$  at  $t_* \leq 1$ . The Mach stem accelerates the interface at  $t_* = \hat{t}_* \approx d/L$ . Since  $\hat{t}_*$  in the present cases ranges from 0.45 to 0.80, the power law of  $a_{s*}$  [34,35] can be expressed by

$$2a_{s*} = C_a t_*^{-3/2}, \quad (23)$$

with a model constant  $C_a$ .

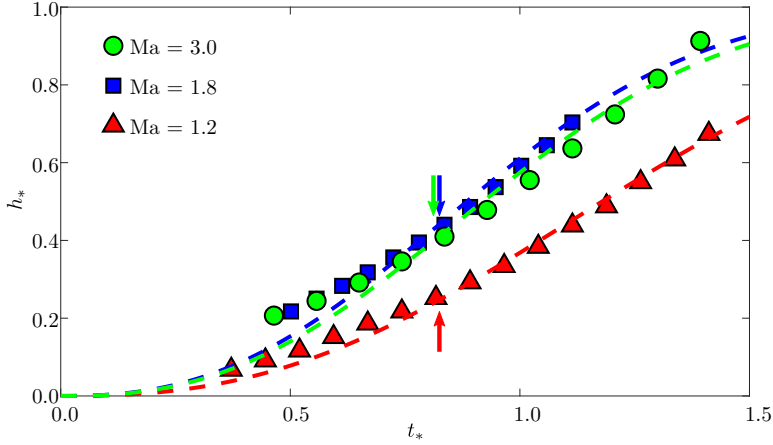


FIG. 15. Evolution of the dimensionless Mach-stem height from DNS (symbols) and modeling (lines) results at various  $Ma$ . The arrow denotes the cavity formation time when the shock first accelerates the interface with  $A = 0.68$  and  $d = 45$  mm. Note that  $t_* = 0$  denotes the initial time when the initial sinusoidal shock has the distance  $d$  from the interface.

Substituting Eq. (23) into Eq. (22) yields

$$\dot{h}_* = t_*^{3/2}(1 - h_*) \frac{1}{C_a} \left( 1 - \frac{Ma_1}{Ma \cos \theta} \right). \quad (24)$$

Then we model

$$C'_h = \frac{1}{C_a} \left( 1 - \frac{Ma_1}{Ma \cos \theta} \right) \quad (25)$$

in Eq. (24) as a constant. This is a strong approximation because  $Ma$  is a constant and  $\theta$  has small variations, whereas  $Ma_1$  is hard to estimate, so it will be examined by the DNS result below. Under this approximation, Eq. (24) can be integrated to obtain

$$h_* = 1 - \exp(-C_h t_*^{5/2}), \quad (26)$$

where the empirical constant  $C_h = 2C'_h/5$  can be fitted from data.

The model in Eq. (26) is validated by a separate DNS of air at  $Ma = 1.2, 1.8,$  and  $3.0$ . The model parameters  $C_h = 0.459$  for  $Ma = 1.2$ ,  $0.942$  for  $Ma = 1.8$ , and  $0.854$  for  $Ma = 3.0$  are fitted from the DNS results, where the Mach-stem height in the DNS is measured from the distance between two triple points in the schlieren contour, and the triple point is identified as the intersection point of the reflected shock and the incident shock [36]. In Fig. 15, the model can well capture the growth of  $h_*$  with  $t_*$ , i.e., it is able to estimate the cavity width in the linear stage with  $k\Delta Ut \leq 1$  in Fig. 9. The good agreement also supports the model approximation in Eq. (25). The model can be extended to a broader parameter space by considering the deformation of the Mach stem [37] and using the power law for nonideal gas [35].

Moreover, this model explains the expansion of slipstreams. Referring to Fig. 4(b), the slipstreams from the light to the heavy gas expand after the Mach-reflection shock accelerating the interface. This is because  $a_{y*}$  decays instantaneously due to the compression effect, and then  $\dot{h}_*$  grows instantaneously according to Eq. (22).

## V. CONCLUSIONS

We distinguish the effects of the interfacial vorticity ( $\omega_{IF}$ ) and the shock-induced vorticity ( $\omega_{CS}$  and  $\omega_{SS}$ ) on the formation of the cavity on a planar interface subjected to a perturbed shock, and demonstrate the important role of the slipstream vorticity ( $\omega_{SS}$ ). Thus, the cavity width in the linear stage depends on the motion of the Mach-reflection shock.

The present instability arises from a perturbed shock at  $Ma = 1.2, 1.8, \text{ or } 3.0$  accelerating a planar light-heavy (air-SF<sub>6</sub>) interface at  $A = 0.30, 0.67, \text{ or } 0.80$ . Its 2D DNS is validated by the experiment result [18]. From the evolution of vorticity and schlieren fields, we define the interfacial and shock-induced vorticities.

To distinguish the roles of each vorticity, we first only vary the interfacial vorticity by artificially modifying the molar mass of SF<sub>6</sub>, and find that  $\omega_{IF}$  has a very slight influence on the cavity width in the linear stage. Thus, the cavity formation is mainly triggered by the shock-induced vorticity. Then, we only vary the initial distance between the incident shock and the interface, and find that the cavity width is determined by the Mach-stem height when the shock accelerates the interface. More specifically, two vorticity patches  $\omega_{SS}$  connecting the Mach stem, as a part of the shock-induced vorticity, penetrate the interface to form the cavity via strong shear layers associated to  $\omega_{SS}$ . Inspired by this mechanism, we develop a model of the Mach-stem height to estimate the cavity width in the linear stage.

The present work focuses on the early stage of the cavity evolution. Future work can be extended to the later stage of the cavity evolution, the effects of reshocks, and different geometric configurations such as cylindrical and spherical geometries.

## ACKNOWLEDGMENTS

Numerical simulations were carried out on the TH-2A supercomputer in Guangzhou, China. This work has been supported by the National Natural Science Foundation of China (Grants No. 11988102, No. 11925201, and No. 91852207), the National Key R&D Program of China (Grant No. 2020YFE0204200), and the Xplore Prize.

- 
- [1] D. Ranjan, J. Oakley, and R. Bonazza, Shock-bubble interactions, *Annu. Rev. Fluid Mech.* **43**, 117 (2011).
  - [2] J. Yang, T. Kubota, and E. E. Zukoski, Applications of shock-induced mixing to supersonic combustion, *AIAA J.* **31**, 854 (1993).
  - [3] D. Arnett, The role of mixing in astrophysics, *Astrophys. J. Suppl.* **127**, 213 (2000).
  - [4] J. D. Lindl, O. L. Landen, J. Edwards, E. I. Moses, J. Adams, P. A. Amendt, N. Antipa, P. A. Arnold, L. J. Atherton, S. Azevedo, D. Barker, M. A. Barrios, I. Bass, S. H. Baxamusa, and NIC Team, Review of the National Ignition Campaign 2009–2012, *Phys. Plasmas* **21**, 020501 (2014).
  - [5] R. D. Richtmyer, Taylor instability in shock acceleration of compressible fluids, *Comm. Pure Appl. Math.* **13**, 297 (1960).
  - [6] E. E. Meshkov, Instability of the interface of two gases accelerated by a shock wave, *Fluid Dyn.* **4**, 101 (1972).
  - [7] Y. Zhou, T. T. Clark, D. S. Clark, S. G. Glendinning, M. A. Skinner, C. M. Huntington, O. A. Hurricane, A. M. Dimits, and B. A. Remington, Turbulent mixing and transition criteria of flows induced by hydrodynamic instabilities, *Phys. Plasmas* **26**, 080901 (2019).
  - [8] Y. Zhou, R. J. Williams, P. Ramaprabhu, M. Groom, B. Thornber, A. Hillier, W. Mostert, B. Rollin, S. Balachandar, P. D. Powell, A. Mahalov, and N. Attal, Rayleigh-Taylor and Richtmyer-Meshkov instabilities: A journey through scales, *Physica D* **423**, 132838 (2021).
  - [9] M. Brouillette, The Richtmyer-Meshkov instability, *Annu. Rev. Fluid Mech.* **34**, 445 (2002).

- [10] Y. Zhou, Rayleigh-Taylor and Richtmyer-Meshkov instability induced flow, turbulence, and mixing. I, *Phys. Rep.* **720**, 1 (2017).
- [11] Y. Zhou, Rayleigh-Taylor and Richtmyer-Meshkov instability induced flow, turbulence, and mixing. II, *Phys. Rep.* **723**, 1 (2017).
- [12] L. Zou, J. Liu, S. Liao, X. Zheng, Z. Zhai, and X. Luo, Richtmyer-Meshkov instability of a flat interface subjected to a rippled shock wave, *Phys. Rev. E* **95**, 013107 (2017).
- [13] R. Ishizaki, K. Nishihara, H. Sakagami, and Y. Ueshima, Instability of a contact surface driven by a nonuniform shock wave, *Phys. Rev. E* **53**, R5592(R) (1996).
- [14] Y. Liang, J. Ding, Z. Zhai, T. Si, and X. Luo, Interaction of cylindrically converging diffracted shock with uniform interface, *Phys. Fluids* **29**, 086101 (2017).
- [15] L. Zou, M. Al-Marouf, W. Cheng, R. Samtaney, J. Ding, and X. Luo, Richtmyer-Meshkov instability of an unperturbed interface subjected to a diffracted convergent shock, *J. Fluid Mech.* **879**, 448 (2019).
- [16] Z. Zhai, Y. Liang, L. Liu, J. Ding, X. Luo, and L. Zou, Interaction of rippled shock wave with flat fast-slow interface, *Phys. Fluids* **30**, 046104 (2018).
- [17] W. Zhang, Q. Wu, L. Zou, X. Zheng, X. Li, X. Luo, and J. Ding, Mach number effect on the instability of a planar interface subjected to a rippled shock, *Phys. Rev. E* **98**, 043105 (2018).
- [18] S. Liao, W. Zhang, H. Chen, L. Zou, J. Liu, and X. Zheng, Atwood number effects on the instability of a uniform interface driven by a perturbed shock wave, *Phys. Rev. E* **99**, 013103 (2019).
- [19] N. J. Zabusky, Vortex paradigm for accelerated inhomogeneous flows: Visiometrics for the Rayleigh-Taylor and Richtmyer-Meshkov environments, *Annu. Rev. Fluid Mech.* **31**, 495 (1999).
- [20] J. W. Jacobs and J. M. Sheeley, Experimental study of incompressible Richtmyer-Meshkov instability, *Phys. Fluids* **8**, 405 (1996).
- [21] N. Peng, Y. Yang, J. Wu, and Z. Xiao, Mechanism and modelling of the secondary baroclinic vorticity in the Richtmyer-Meshkov instability, *J. Fluid Mech.* **911**, A56 (2021).
- [22] N. Peng, Y. Yang, and Z. Xiao, Effects of the secondary baroclinic vorticity on energy cascade in the Richtmyer-Meshkov instability, *J. Fluid Mech.* **925**, A39 (2021).
- [23] H. F. Li, Z. W. He, Y. S. Zhang, and B. L. Tian, On the role of rarefaction/compression waves in Richtmyer-Meshkov instability with reshock, *Phys. Fluids* **31**, 054102 (2019).
- [24] J. Ge, H. F. Li, X. T. Zhang, and B. L. Tian, Evaluating the stretching/compression effect of Richtmyer-Meshkov instability in convergent geometries, *J. Fluid Mech.* **946**, A18 (2022).
- [25] E. F. Toro, *Riemann Solvers and Numerical Methods for Fluid Dynamics* (Springer-Verlag, Berlin, 2009).
- [26] Y. Yang, Q. Zhang, and D. H. Sharp, Small amplitude theory of Richtmyer-Meshkov instability, *Phys. Fluids* **6**, 1856 (1994).
- [27] W. Xiao, M. Andrae, and N. Gebbeken, Development of a new empirical formula for prediction of triple point path, *Shock Waves* **30**, 677 (2020).
- [28] W. Mostert, D. I. Pullin, R. Samtaney, and V. Wheatley, Singularity formation on perturbed planar shock waves, *J. Fluid Mech.* **846**, 536 (2018).
- [29] A. Rikanati, O. Sadot, G. Ben-Dor, D. Shvarts, T. Kuribayashi, and K. Takayama, Shock-Wave Mach-Reflection Slip-Stream Instability: A Secondary Small-Scale Turbulent Mixing Phenomenon, *Phys. Rev. Lett.* **96**, 174503 (2006).
- [30] G. Emanuel, Vorticity in unsteady, viscous, reacting flow and downstream of a curved shock, *AIAA J.* **45**, 2097 (2007).
- [31] A. Cachucho and B. W. Skews, Guderley reflection for higher Mach numbers in a standard shock tube, *Shock Waves* **22**, 141 (2012).
- [32] L. F. Wang, C. Xue, W. H. Ye, and Y. J. Li, Destabilizing effect of density gradient on the Kelvin-Helmholtz instability, *Phys. Plasmas* **16**, 112104 (2009).
- [33] C. A. Mouton and H. G. Hornung, Mach stem height and growth rate predictions, *AIAA J.* **45**, 1977 (2007).
- [34] G. Fraley, Rayleigh-Taylor stability for a normal shock wave-density discontinuity interaction, *Phys. Fluids* **29**, 376 (1986).
- [35] J. W. Bates, On the theory of a shock wave driven by a corrugated piston in a nonideal fluid, *J. Fluid Mech.* **691**, 146 (2012).

- [36] H. Wang, Z. Zhai, and X. Luo, Prediction of triple point trajectory on two-dimensional unsteady shock reflection over single surfaces, *J. Fluid Mech.* **947**, A42 (2022).
- [37] X. Shi, Y. Zhu, J. Yang, and X. Luo, Mach stem deformation in pseudo-steady shock wave reflections, *J. Fluid Mech.* **861**, 407 (2019).